Engineering Structures 317 (2024) 118633

Contents lists available at ScienceDirect

Engineering Structures

journal homepage: www.elsevier.com/locate/engstruct

Analysis of the performance of GNSS receiver in monitoring the behaviour of the wind turbine nacelle

Chenyu Xue [a], Panos A. Psimoulis [a], Craig Hancock [b,*], Francis Xavier Ochieng [c], Yuchen Yang [d], Chendong Li [e], Paul Bhatia [f], Yiru Li [g], Xu Tang [h]

[a] *Nottingham Geospatial Institute, University of Nottingham, Nottingham, UK*
[b] *Loughborough University, Loughborough, UK*
[c] *Jomo Kenyatta University of Agriculture and Technology, Kenya*
[d] *University of Nottingham, Ningbo, China*
[e] *Zhejiang Normal University, China*
[f] *Geomatic Ventures Limited, Nottingham, UK*
[g] *University College London, London, UK*
[h] *Nanjing University of Information Science and Technology, Nanjing, China*

ARTICLE INFO

Keywords:
Wind turbine
Nacelle
Structural health monitoring
GNSS
Timeseries
Multipath
Geometric constraint

ABSTRACT

Wind turbines are frequently employed to harness the kinetic energy of the wind for electricity generation, and they are anticipated to encounter diverse wind forces that could lead to potentially severe structural reactions. Hence, structural health monitoring is an essential task for safe and productive operation of wind turbines. The structural health monitoring of wind turbines is usually conducted using strain gauges, accelerometers, etc., while few studies have applied Global Navigation Satellite System (GNSS) technology for monitoring the response of wind turbines. This study is the first attempt to evaluate the performance of GNSS receivers in monitoring the behaviour of the nacelle of a wind turbine. For the purpose of this study, we conducted experiments where the position and behaviour of the nacelle was recorded by an array of GNSS receivers strategically positioned on a wind turbine nacelle. A GNSS base station was used for post-processing the GNSS raw data and the GNSS time-series were analysed to evaluate the GNSS receivers' performance. Two experiments were conducted. In the first experiment, we evaluated the performance of the GNSS receivers depending on their position on the nacelle and analysed of the precision of the estimation of nacelle position and orientation. In the second experiment, we assessed the GNSS performance under different configurations of nacelle and turbine blade movements, considering scenarios where the nacelle was either stationary or subjected to rotation, and the turbine blades were either stationary or in motion. As the first pioneering study in wind turbine nacelle monitoring with GNSS, in the study, we present the main results of the performance of GNSS receivers in monitoring the behaviour of the nacelle of wind turbine and we develop methodologies in GNSS data analysis to enhance the precision of the GNSS time-series. The study revealed a planar precision range of 5–7 mm during blade rotation, improving to 4–6 mm when the blade slows or stops, alongside a high precision of 1.6 degrees for nacelle bearing determination using GNSS coordinates.

1. Introduction

Wind turbines are key components of renewable energy and play an important role in reaching net zero strategies, which further contribute to mitigating the impact of climate change. Growing wind farm numbers not only require installing turbines but also demand a robust framework for sustainable monitoring and maintenance to ensure operational availability and reliability. Implementing continuous Structural Health Monitoring (SHM) is essential for wind farm managers in ensuring optimal performance, providing early fault detection, and enabling timely maintenance which significantly enhances the entire life cycle of the wind turbines. With the advancement and optimisation of wind turbine technology, the wind turbines nowadays are more structurally flexible, presenting challenges due to varying modal frequencies [1].

---

[*] Corresponding author.
E-mail addresses: chenyu.xue@nottingham.ac.uk (C. Xue), panagiotis.psimoulis@nottingham.ac.uk (P.A. Psimoulis), c.m.hancock@lboro.ac.uk (C. Hancock).

https://doi.org/10.1016/j.engstruct.2024.118633
Received 16 February 2024; Received in revised form 21 June 2024; Accepted 14 July 2024

Empirical SHM studies conducted regarding wind turbines are primarily for the blades, tower and wind turbine foundation, where the structural dynamic responses such as strain, fatigue, and modal property are monitored and derived by a combination of different sensors, such as strain gauges [2], Linear Variable Differential Transformer (LVDT) [3], accelerometers [4], piezoelectric transducers [5], micro-electromechanical system (MEMS) [6], and Fiber Bragg Grating (FBG) [7].

For instance, Ou, et al. [8] employed a set of accelerometers on a small wind turbine blade with the aim to detect damage through the acquired response signals using appropriate statistical and modal analysis. Barber, et al. [9] designed a cost-effective self-sustaining wind turbine blade SHM system using MEMS incorporating several different sensors including inertial measurement unit (IMU), pressure sensor, and acoustic sensor, etc. Smarsly, et al. [10] also installed the SHM system on an onshore wind turbine for the steel tower and foundation monitoring, including anemometers mounted on the nacelle; accelerometers, displacement transducers and temperature detectors installed in the tower and seismic accelerometers placed at the foundation.

With the development of Global Navigation Satellite System (GNSS) technology for the past few decades, GNSS could reach mm-level accuracy by using a rover-reference receiver formation and employing post-processing kinematic technique, which could be a competitive candidate for structural health monitoring [11–13]. According to Yu, et al. [14], SHMs were already implemented with GNSS for civil engineering infrastructures either by real-time kinematic (RTK) [15] or postprocessing kinematic (PPK) [16] and had been proven mature over last two decades.

However, GNSS technology has seen very little integration with wind turbines, especially much less in SHM applications. Maes, et al. [17] conducted the motion tracking of a wind turbine blade using RTK GPS when the turbine blade was hoisted. Ren, et al. [18] estimated the wind turbine hub displacement for offshore wind turbine in real time using an integrated GNSS and IMU. But these two studies are both regarding the turbine installation stage and the displacements are due to human factors. Caterino, et al. [19] conducted an evaluation of GNSS technology's feasibility for monitoring wind turbine structures. They performed a series of numerical simulations using a wind turbine case study to quantitatively evaluate whether GNSS was feasible for structural control of wind turbines. Rossi, et al. [20] also simulated the motion of a wind turbine using a robot with the aim of tracking its motion with GNSS. In their study, the GNSS antenna and receiver were mounted on the robot executing translation and rotation motions. These two studies demonstrated the potential of GNSS in monitoring wind turbine movement through numeric data simulation. Nevertheless, neither of the research has applied GNSS receivers directly on real-world wind turbine monitoring projects.

Therefore, in this study, we placed four strategically arranged GNSS antennas on a bracket fixed to the nacelle of a small wind turbine, to evaluate the performance of GNSS receivers in the challenging conditions of wind turbine monitoring, where the periodic rotation of the wind turbine blades create periodical obstructions and repeated strong multipath conditions [21]. The study did not aim to evaluate GNSS performance in monitoring wind turbine and nacelle deformation (either dynamic or slow), but rather focused on assessing GNSS precision in monitoring the kinematic behaviour of the nacelle (i.e. positioning and orientation). For this purpose, this study focused on the evaluation of the precision and performance of the GNSS receivers (i) depending on the relative position of the GNSS antenna on the nacelle, and (ii) regarding the operational states of the wind turbine. (i.e. either a stationary condition or rotational movement of the nacelle, coupled with either stationary or circular motion of the wind turbine blades). Furthermore, this study focuses on the development of methods to enhance the GNSS time-series precision for position and orientation estimation of the wind turbine nacelle. The performance evaluation of the GNSS receivers was based on two controlled experiments by monitoring the nacelle under various operational states of wind turbine, where four GNSS receivers were deployed on the nacelle of a wind turbine and recording the position and behaviour of the wind turbine nacelle.

This paper is structured as follows, firstly, the experiment is introduced in Section 2. In Section 3, the GNSS timeseries processing and analysis procedure is proposed, and in Section 4, the results of the GNSS are presented, together with accuracy improvement strategies incorporating the multiple antennas, the GNSS measurement errors are also analysed based on four different nacelle and turbine blade movement cases. And finally, the results are discussed, and the conclusions are made for generalisation of wind turbine monitoring.

2. Experimentation

The experiment was carried out by using a small wind turbine (specification in Table 1), manufactured by Zhejiang WinPower Energy Technology Co Ltd (China), at the University of Nottingham Ningbo China (UNNC) on 18/08/2020. The equipment was mounted as shown in Fig. 1. The T-shaped metal frame was fixed rigidly on top of the nacelle and followed potential rotational movement of the nacelle. The wind turbine blades could execute circular motion in the vertical plane, with a logger recording the total number of rotations in the vertical plane, while the nacelle could rotate in the horizontal plane.

Four GNSS antennas were mounted on the metal frame; three GNSS antennas were mounted at the three arm-ends of the metal frame and one GNSS receiver at the connection-centre of the T-shaped metal frame (Fig. 2). The distance of each arm-end from the centre of the frame was 0.4 m. Three GNSS stations were consisted of Leica GS10 GNSS receivers connected to Leica AS10 GNSS antennas, labelled as sd1, sd2, sd3, whereas one GNSS station was consisted of Javad GNSS receiver and antenna. For the two experimental sessions, two different deployments of the GNSS stations were applied; (i) for the first session, the equipment was arranged as Fig. 3a and the GNSS measurements were carried out from around 07:00:00 to around 08:30:00 GPST; (ii) the second session was arranged similarly according to the plan on Fig. 3b, and the measurement was carried out on about 09:21:00 to 10:40:00 GPST. The GNSS receivers were recording with a 10 Hz sampling rate by tracking satellites signal of from GPS, GLONASS and Galileo. A base station consisted of a Leica GR10 receiver and AR 25 antenna was established on the roof of Science and Engineering Building (SEB) in UNNC, also recording GPS, GLONASS and Galileo signals. The baseline distance between rover and base was ~360 m. The Javad receiver did not record

Table 1
Wind turbine parameters.

Model	Horizontal-axis small wind turbine FS-300
Type	Onshore
Rated voltage (V)	24 / 12
Rated output power (W)	300
Blade material & quantity	Aluminium alloy -three blades
Wheel diameter (m)	2
Start-up wind speed (m/s)	2
Cut-in wind speed (m/s)	3
Rated wind speed (m/s)	10
Safety wind speed (m/s)	35
Working temperature (°C)	−40 to 50
Turbine weight (kg)	32
Generator Type	three-phase AC synchronous permanent magnet
Controlling	Dump load; automatically adjusting to headwind; electromagnetic/manual brake

Fig. 1. The wind turbine and the layout of the GNSS antennas as mounted for the first experimental session.

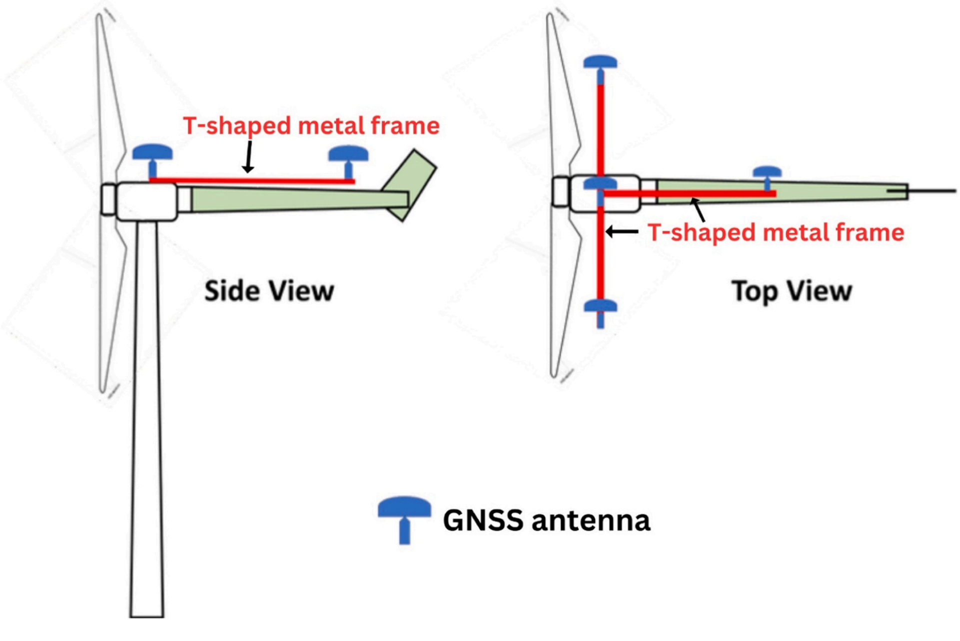

Fig. 2. Schematic drawing of the wind turbine from side view and top view with the layout of the GNSS sensors.

any data during both sessions; therefore, Javad measurements were not included in the data analysis.

In the first experimental session, the nacelle and the blades of the wind turbine were rotating freely, depending on the wind direction and speed, whereas in the second experimental session, four different scenarios of the nacelle and wind turbine behaviour (i.e. either free or no rotation-yaw motion of the nacelle paired with either free or no rotation of the blades) were applied to examine the errors of the GNSS measurements for various cases of operational modes of the wind turbine and study how the kinematic behaviour of the nacelle and blades affects the GNSS measurements. The wind on the day was moderate with an average speed of around 18–25 kph (from 07:00–11:00 GPST) [22]. The GNSS raw data were collected on the memory (SD cards) of the Leica receivers, recording triple frequency GNSS measurements.

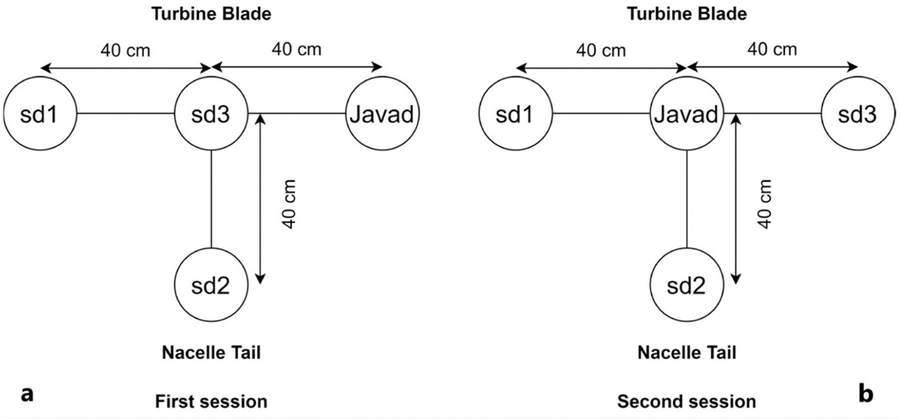

Fig. 3. The layout of the four GNSS antennas mounted on the metal frame for the two experiments.

3. GNSS data processing and methodology

The data of the GNSS receivers of the wind turbine and the base station were converted to RINEX format and post-processed using post-processing kinematic (PPK) technique. The PPK was a double difference method, where the GNSS base station was used as reference station to cancel or largely mitigate the common errors, such as satellite orbit error, receiver errors, ionospheric and tropospheric errors, etc., between the GNSS base station and the GNSS receivers of the wind turbine. This meant that the GNSS residual error sources would mainly be due to multipath effect and dilution of precision caused by the relative geometry of the receiver-satellite [21] and potential unmitigated ionospheric and tropospheric error, and white noise [16].

For the process of the GNSS data, the RTKPOST module of the open-source software RTKLIB [23] was used, with the solution settings shown in Table 2. For monitoring purposes, only the displacement of the wind turbine, which was expressed as the relative movement with respect the base station, was computed [12,24]. Therefore, the results were expressed in E/N/U baseline solutions, with the baseline distance projected onto local E/N/U directions and the reference station as the origin. The results for the first session of the experiment were shown as a timeseries in Fig. 4 and Fig. 5, where the E/N/U GNSS timeseries and wind turbine rotation logger data were used. Regarding the time scale (x-axis), a common timestamp was used with the starting point ($t = 0$) as reference for all timeseries of the three stations. The coordinates in y-axis were offset on purpose for a clearer view of the data.

Based on the obtained 10-Hz E/N/U GNSS timeseries we analysed the performance of the GNSS receivers in monitoring the wind turbine nacelle behaviour. More specifically, for the first experiment we analysed:

1) the precision of the position estimation of the GNSS receivers, depending on their position on the wind turbine nacelle,
2) the precision of the orientation estimation of the nacelle based on the analysis of the three GNSS time-series their geometric relationship.
3) the potential enhancement of the estimated position and orientation of the wind turbine nacelle by analysing the GNSS time-series and applying the geometric constraints between the GNSS receivers.

For the second experiment we analysed the performance of the GNSS time-series for various scenarios of nacelle motion and rotation of the wind turbine blades.

Table 2
RTKLIB settings.

RTKPOST options	Settings
Position mode	Kinematic
Frequency	L1 +L2
Filter type	Combined
Elevation Mask	15 degrees
Receiver dynamics/Ocean tide corrections	Off
Ionosphere correction	Broadcast
Satellite ephemeris/Clock	Broadcast
Troposphere correction	Saastamoinen
Navigation System	GPS only
Ambiguity Resolution	Continuous
Min Ratio to fix ambiguity	3

4. Data analysis

The preliminary analysis of the E/N GNSS timeseries (Fig. 4) showed that the GNSS receivers sd1 and sd2 were executing periodic movement, with the amplitude reaching about 0.8 m, which practically corresponded to the circular motion of the nacelle. However, for GNSS timeseries of sd3, as it was at (or very close to) the rotation centre of the nacelle, the range of E/N was only below 0.1 m representing GNSS measurement errors. In Fig. 5, the Up timeseries was depicted, with the green line indicating the transient rotation speed, calculated as the gradient of the number of rotations with respect to time. It was observed in Fig. 5 that the high rotation speed occurring between 1000 s and 2000 s correlated to the larger spread of the Up component of GNSS timeseries, indicating lower GNSS precision. From Fig. 5, it was revealed that the sd3 GNSS receiver had the lower precision compared to sd1, while the sd2 receiver seemed to have the most precise performance. This could be justified by the location of the GNSS antennas and the impact of the rotation of the wind turbine blades, since the sd2 receiver was the furthest away from the wind turbine blades, and the sd3 receiver was at the centre on the nacelle where the multipath effect was significant coming from both side of the blade rotation, whereas the sd1 receiver was only influenced partially as it was on the left side of the nacelle.

4.1. Precision analysis

In Fig. 6, the N-E trajectory of the nacelle movement for sd1 and sd2 was shown, where an obvious circular shape could be observed from the scatter, representing the trajectory regarding the rotation centre of the nacelle. The radius of the circle was around 0.4 m, corresponding to the distance from sd1 to sd3 and sd2 to sd3, as the receiver sd3 could be considered practically at the centre of nacelle rotation motion. The uneven distribution of the scatter points meant that the nacelle mainly oscillated in a limited azimuth range.

Furthermore, a circular fit was applied on the Easting-Northing trajectory data based on least squares using the Pratt method [25] for the sd1 and sd2 timeseries data between the period of 2100 s to 4000 s, since the wind turbine blade rotations were few during that time period,

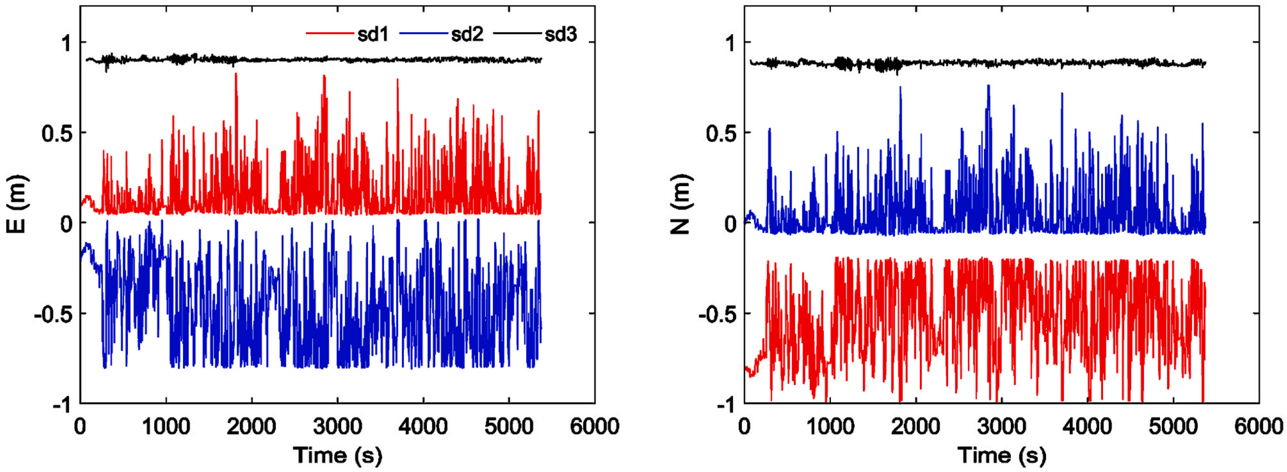

Fig. 4. Easting/Northing timeseries for the first measurement session for sd1, sd2, and sd3 stations.

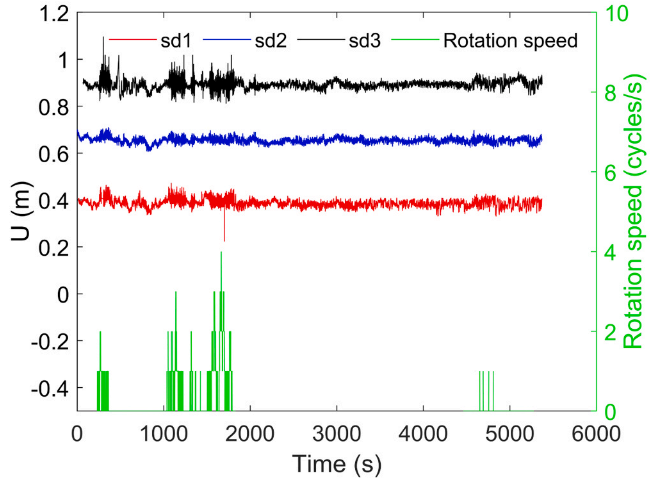

Fig. 5. Up components for sd1, sd2, and sd3 in correlation with the rotation speed for the first measurement session.

which consequently resulted in reduced multipath-induced noise. By using the circular fitting, the centres and radii of the circle defined by sd1 and sd2 could be estimated. Based on the estimated radius and centre of sd1 and sd2 receivers' data, the precision of the planar (Easting-Northing components) GNSS measurement were computed as the standard deviation of the radius residuals.

The radius residuals timeseries of sd1 and sd2 and the Easting/Northing of sd3 were presented in Fig. 7, where it was confirmed that the standard deviation of the timeseries seemed to be correlated with the rotation speed, e.g., the standard deviation tended to increase with the rotation speed.

Tables 3 and 4 presented the standard deviations of the Up-component of sd1, sd2, sd3 (Fig. 5), and the radial residuals of sd1, sd2 and Northing/Easting component of sd3 (Fig. 7) respectively, for various periods which corresponded to relatively large rotation speed (i.e. 265–390 s, 1050–1250 s, and 1520–1820 s) and very slow or with no rotation speed (i.e.2100 −4100 s). The standard deviation expressed the range of the residuals and corresponded to data noise. The results of Tables 3 and 4 confirmed the outcome of Figs. 4 and 6, that the receiver at sd3 was less precise relatively to the other two receivers for both horizontal and vertical components and that sd2 was more precise than sd1.

We computed the timeseries of horizontal distances by establishing three pairs among the three receivers (sd1, sd2, and sd3) using their Easting and Northing measurements. The distances between sd1/sd2 to sd3 were predetermined and fixed at 0.4 m, based on the dimensions of the metal bracket used for receiver installation on the nacelle. We assessed the accuracy and precision of distance measurements by calculating accuracy as the variance between the average distance estimation and the known-fixed distances value. Precision was

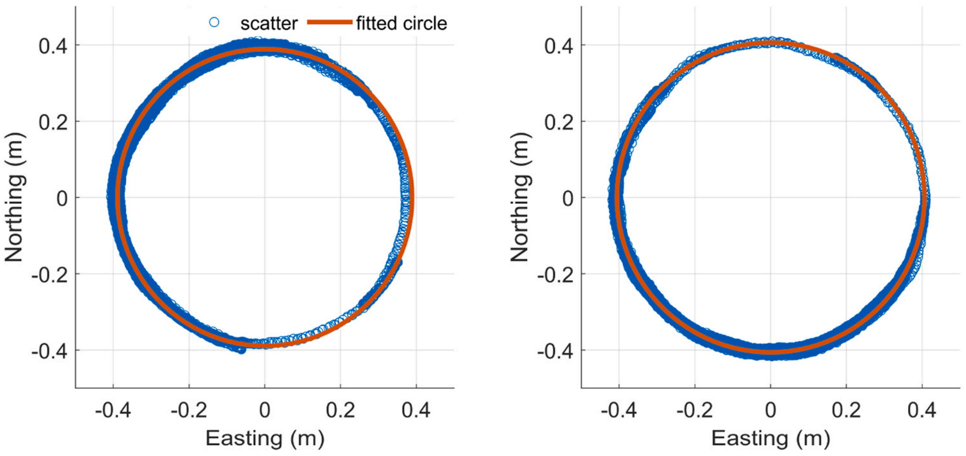

Fig. 6. Northing vs Easting for sd1 (left) and sd2 (right) for the first measurement session (The red circular curve is the circular fit based on the scattered measurements).

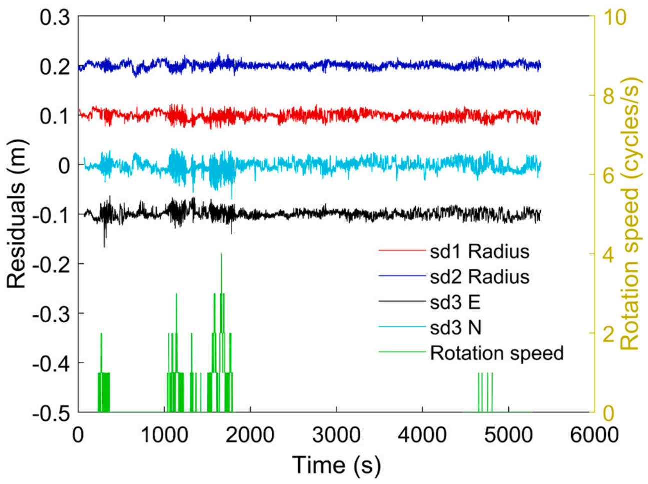

Fig. 7. sd1 and sd2 radius residual and sd3 E/N residual in correlation with the rotation speed.

Table 3
Standard deviation of Up timeseries for each period (unit: mm). The first three columns correspond to fast blade rotation and the last column corresponds to a relative slow blade rotation.

Up (in mm)	265-390 s	1060-1250 s	1520-1820 s	2100-4000 s
sd1	14	14	15	11
sd2	11	11	10	9
sd3	28	23	22	11

Table 4
Similar to Table 3 for the planar precision (unit: mm).

	265-390 s	1060-1250 s	1520-1820 s	2100-4000 s
Radius Residual (in mm)				
sd1	7	6	7	6
sd2	5	5	6	4
E/N (in mm)				
E sd3	10	10	8	5
N sd3	13	9	13	8

determined as the standard deviation of the distance's residuals, derived from the differences between the estimated distances and the fixed distances.

Table 5 presented the accuracy and the precision for distance calculation of sd1-sd2, sd2-sd3, and sd1-sd3. Based on the calculated accuracy and precision, the accuracy of the distances related to the sd3 GNSS receiver was lower, since the error of the distances sd1-sd3 and sd2-sd3 were 23 mm and 11 mm, respectively, whereas the error of sd1-sd2 was only 1 mm. The larger errors in the distances with respect to sd3 were due to larger noise level of E/N GNSS coordinates of sd3, indicated also in Fig. 5 and Fig. 7, based on which the corresponding distances (sd1-sd3 and sd2-sd3) were calculated. The precisions of all distances similarly ranged between 5 to 8 mm.

Table 5
Statistic table for distance of sd1 to sd3, sd2 to sd3, and sd1 to sd2. The precision and accuracy were expressed as standard deviation and deviation from the true value, respectively.

	Average (mm)	Standard deviation (mm)	True value (mm)	Error (mm)
sd1-sd3	377	8	400	−23
sd2-sd3	411	5	400	11
sd1-sd2	564	7	565	−1

4.2. Nacelle orientation analysis

The second parameter analysed was the orientation of the nacelle, determined as (i) the azimuth of the nacelle defined based on the Easting-Northing measurements of sd2 and sd3 receivers, and (ii) the azimuth of the axis defined by sd1 and sd3 receivers (metal bracket) which was parallel to the rotation plane of the turbine blade. The orientation in both cases was computed as the azimuth of sd2 to sd3 and sd1 to sd3 based on Eq. 1:

$$Azimuth = \arctan\frac{\Delta E}{\Delta N} \tag{1}$$

where ΔE and ΔN were the difference between the receivers (sd1 and sd3 or sd2 and sd3) in Easting and Northing.

In Fig. 8, the azimuth from sd2 to sd3 and from sd1 to sd3 was presented as timeseries, with 0 degrees corresponding to the North, ± 180 degrees to the South, 90 degrees to the East, and −90 degrees to the West. Notably, significant oscillations occurred around 0 degrees for sd2 to sd3, indicating frequent nacelle oscillations around the North/South axis. Additionally, the geometry among the three receivers established a correlation between the azimuth formed by sd2 to sd3 and that formed by sd1 to sd3, governed by the rigid metal arm. This correlation was expressed in Eq. 2:

$$Azimuth_{sd1to\ sd3} = Azimuth_{sd2to\ sd3} + \frac{\pi}{2} \quad (\mathrm{unit:radians}) \tag{2}$$

Utilizing Eq. 2, the azimuth of sd1 to sd3 can be derived from the azimuth of sd2 to sd3. Consequently, the disparity between the azimuth of sd2 to sd3 obtained through coordinate computation and the azimuth of sd2 to sd3 computed from that of sd1 to sd3 can be quantified. Fig. 9 illustrated the residuals of the nacelle azimuth, representing the difference between these two azimuth calculations involving the three receivers—sd1, sd2, and sd3.

The observed azimuth residuals predominantly fluctuated within the range of −5 to 5 degrees. However, during periods of elevated rotation speed of the turbine blade, there was an escalation in the variability of residuals, indicating the influence of data noise on the estimation of nacelle azimuth. Specifically, the standard deviation from 1000 to 2000 s, corresponding to heightened wind turbine blade movement, was 1.8 degrees. In contrast, during intervals from 3000 to 4000 s, associated with minimal or no turbine rotation, the standard deviation reduced to 1.3 degrees (as shown in Fig. 9).

4.3. Positioning analysis based on geometrical constraints

The position of the GNSS receiver sd3 can be estimated by using the position of the GNSS receivers at sd1 and sd2 and the geometric constraints between the three receivers. Based on the geometry of the bracket for setting up the GNSS receivers, the GNSS receivers formed a right angle with equal distances between sd1 to sd3 and sd2 to sd3. Based on the distances and orientation of the GNSS receivers (Fig. 10), the Easting and Northing of sd3 can be expressed as function of the location of GNSS receivers sd2, sd1 and their relative distances and azimuths, by using following Eqs. 3 and 4:

$$\begin{aligned} E_{sd3}{}'' &= E_{sd2} + l_{sd2to\ sd3} * \sin(Azimuth_{sd2to\ sd3}) N_{sd3}{}'' \\ &= \quad N_{sd2} + l_{sd2to\ sd3} * \cos(Azimuth_{sd2to\ sd3}) \end{aligned} \tag{3}$$

$$\begin{aligned} E_{sd3}{}' &= E_{sd1} + l_{sd1to\ sd3} * \sin(Azimuth_{sd1to\ sd3}) N_{sd3}{}' \\ &= \quad N_{sd1} + l_{sd1to\ sd3} * \cos(Azimuth_{sd1to\ sd3}) \end{aligned} \tag{4}$$

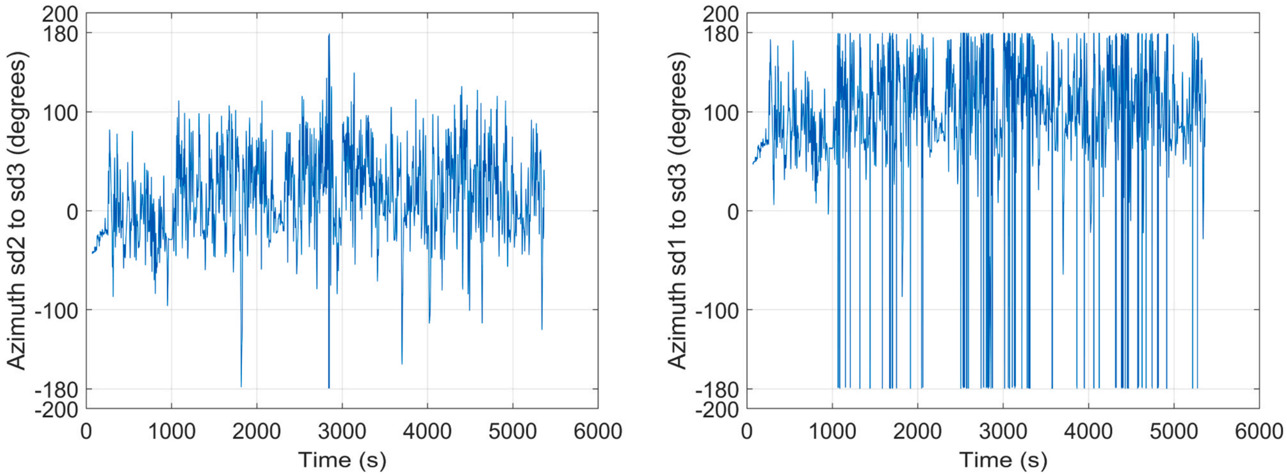

Fig. 8. Azimuth from sd2 to sd3 in degrees (left) and azimuth from ad1 to sd3 (right).

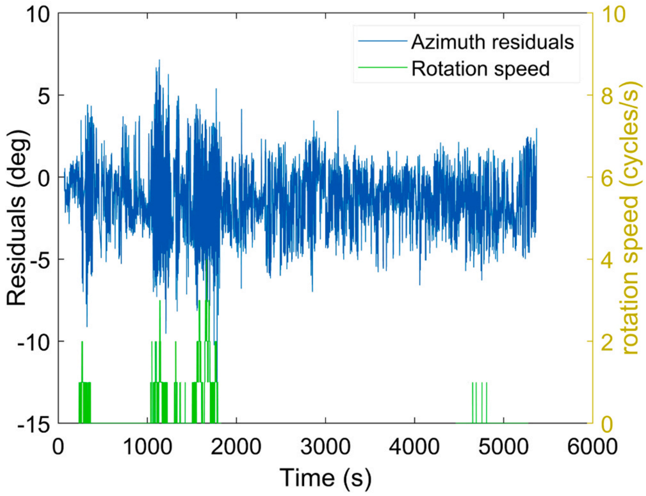

Fig. 9. The azimuth residuals based on the fixed angle relationship between sd2 to sd3 and sd1 to sd3.

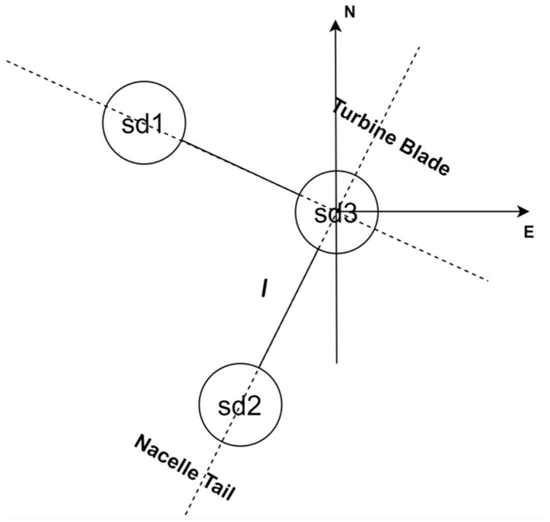

Fig. 10. The Easting/Northing relationship between sd2 and sd3 stations & sd1 and sd3 stations based on bearings and distances.

where E_{sd1} N_{sd1} , E_{sd2} N_{sd2} were the Easting and Northings of sd1 and sd2 receivers, respectively; and $l_{sd2to\ sd3}$ $l_{sd1to\ sd3}$ and $Azimuth_{sd2to\ sd3}$ $Azimuth_{sd1to\ sd3}$ were the distances and azimuths between sd2-sd3 and sd1-sd3, respectively.

Then, the Easting and Northing of GNSS receiver sd3 can be computed as the weighted average of the Easting and Northing coordinates derived directly from the measurements of GNSS receiver sd3 and the coordinates based on the computations of Equations 3 and 4 and the measurements of GNSS receivers sd2 and sd1, respectively. The weighted average equations of Easting and Northing can be expressed with the following formulae:

$$E_{sd3adj} = \frac{w_E E_{sd3} + w'_E E'_{sd3} + w''_E E''_{sd3}}{w_E + w'_E + w''_E} N_{sd3adj} = \frac{w_N N_{sd3} + w'_N N'_{sd3} + w''_N N''_{sd3}}{w_N + w'_N + w''_N} \tag{5}$$

where the W_E W'_E and W''_E,W_N W'_N and W''_N denoted the weights of each component as they were derived based on the estimated precision of the GNSS receivers sd3, sd1 and sd2, respectively. The weights were calculated all based on the period of 2100 s to 4000 s, where there was less movement from the rotation blade and the standard deviation of the timeseries remained stable. The calculation of the w_E, w'_E, w''_E and w_N w'_N w''_N were as follows (Equation 6), where $\sigma_{\mathrm{RR}_{sd1}}$ and $\sigma_{\mathrm{RR}_{sd2}}$ were the standard deviation of radius residual of sd1 and sd2 respectively.

$$w_E = \frac{1}{\left(\sigma_{\mathrm{E}_{sd3}}\right)^2} \quad w'_E = \frac{1}{\left(\frac{\sigma_{\mathrm{RR}_{sd1}}}{\sqrt{2}}\right)^2} \quad w''_E = \frac{1}{\left(\frac{\sigma_{\mathrm{RR}_{sd2}}}{\sqrt{2}}\right)^2} w_N = \frac{1}{\left(\sigma_{\mathrm{N}_{sd3}}\right)^2} \quad w'_N = \frac{1}{\left(\frac{\sigma_{\mathrm{RR}_{sd1}}}{\sqrt{2}}\right)^2} \quad w''_N = \frac{1}{\left(\frac{\sigma_{\mathrm{RR}_{sd2}}}{\sqrt{2}}\right)^2} \tag{6}$$

Furthermore, apart from using the weighted average for the calculation of the error in sd3 Eastings and Northings, we also calculated the mean average by assuming that all the GNSS measurements were of similar precision and allocating equally weight of 1/3.

As the geometry of the metal frame was known, there were two geometric constraints that could be applied to limit the uncertainty of the GNSS estimation of station sd3 by reducing its standard deviation, as shown in Table 5 and Eq. 2. In Table 5, the distance between sd1 and sd3, and the distance between sd3 and sd2 could either be determined and set to a fixed value, referred to as fixed distance; or still be calculated using the sd1, sd2, sd3 coordinate timeseries referred as unfixed distance. In Eq. 2, the azimuth sd1 to sd3 could be fixed by either using the azimuth of sd2 to sd3 added by π/2, referred to as fixed or by the azimuth calculation using coordinate timeseries of sd1 and sd3 referred to as 'not fixed'.

To evaluate the improvement of using a fixed distance or a known azimuth constraint, four cases were considered: 1) fixed angle, fixed distance. 2)fixed angle, not fixed distance, 3) not fixed distance and not fixed angle, 4) not fixed angle and fixed distance.

Table 6 displayed the outcomes for both weighted average and mean average across various scenarios. Notably, the scenario with a non-fixed angle and fixed distance exhibited the highest precision among the four cases, achieving a precision of 6.6 mm for Easting and 7.9 mm for Northing. Interestingly, the weighted average results showed only marginal improvement in precision compared to the averaged results.

4.4. Analysing the performance of GNSS receivers for various motion modes of the wind turbine nacelle

In the second experiment, we examined the performance of the GNSS receiver for four different modes of operation states of the wind turbine, defined by the movement of the nacelle and the rotation of the blades; (i) case A, where the nacelle was not moving or it was moving very slowly (i.e. no or very little yaw motion of the nacelle) and the blades were not rotating; (ii) case B, where the nacelle was restrained and cannot move (i.e. no yaw motion) but the blades can freely rotate; (iii) case C, where nacelle can freely move (i.e. free yaw motion) but the blades were not rotating; and (iv) case D: where the nacelle can freely move (i.e. free yaw motion) and the blades were rotating. For the cases A and B of the second experimental session, the nacelle was forced to stay still even if the blade was moving. In this experimental session we focused on the analysis of sd2 GNSS receiver, the GNSS receiver positioned at the tail of the nacelle, as it was proved to be location of the nacelle with the lowest impact on the GNSS measurements. Figs. 11 and 12 showed the Easting/Northing/Up timeseries for the four different cases (A-D) for the GNSS receiver at sd2 as well as the rotation blade speed for each case.

For case A, it seemed that there was almost no motion of the nacelle for the time-interval between $t = 3760$ s to $t = 3820$ s, while for the rest of the period there was some slow motion of the nacelle affecting mainly the Easting component with a range of 0.2–0.3 m. There was practically no rotation of the blades which was reflected also by low deviation of the Up time-series ($\sigma = 9.0$ mm). For case B, the nacelle was restrained which resulted to very limited motion, especially for the period up to $t = 500$ s, whereas for the time interval $t = 540$ s to $t = 600$ s, there were some larger deviations of the nacelle expressing a combination of motion and noise produced by the blades rotation as it was expressed in the Up time-series ($\sigma = 8.5$ mm). For the case C, there was no rotation of the blades which resulted to low data noise as expressed in the low deviation of Up time-series ($\sigma = 6.6$ mm) and the nacelle moved freely in Easting and Northing time-series in a range of 0.66 m and 0.21 m, respectively. Finally for the case D, the nacelle was under free rotation and probably subjected to stronger wind as the motion range was about 0.69 m and 0.57 m for Easting and Northing time-series respectively, while the speed rotation of the blades was also high resulting to relatively to highly noisy data in Up time-series ($\sigma = 10.4$ mm).

Figs. 13 and 14 presented spectral analysis of the Easting, Northing and Up time-series using DFT. For the high-frequency range (i.e. >1 Hz) mainly expressing white noise of GNSS data, the larger peaks corresponded to cases B and D, in which turbine blades were rotating. On the contrary, the lower peaks corresponded to cases A and C, in which the blades were not rotating. Furthermore, white noise level was more significant for case D than C, indicating that the white noise level for frequencies > 1 Hz increased with the rotation of the blades due to the GNSS multipath error [21,26]. Also, it seemed that larger white noise level was observed for case D compared to B, and for C compared to A for Easting, probably due to the multipath effect induced predominantly by free motion of the nacelle since the turbine blades were not moving in both cases. On the other hand, for the low-frequencies range (i.e. <1 Hz), the Easting and Northing spectra were a combination of the low-frequency motion of the nacelle and coloured noise of the GNSS time-series (especially for frequencies < 0.1 Hz). It was observed that for the cases C and D, where the nacelle experienced unrestricted movement, the E/N spectra was distinguished by elevated peaks in contrast to cases A and B, where the nacelle remained stationary or exhibited minimal movement.

Table 6
The E/N precision for sd3 considering the sd1 and sd2 measurements for the whole period for four different cases for both weighted average and average.

σ (mm)		Weighted average	Average (1/3 wt)
Both fixed	E	7.9	8.4
	N	8	8.1
Fixed angle	E	8.2	8.5
Not fixed distance	N	9.4	9.4
Not fixed angle	E	6.6	6.7
Fixed distance	N	7.9	8.1
Not fixed angle	E	7.2	7.2
Not fixed distance	N	9.5	9.5

5. Discussion

The first experimental session focused on (i) the analysis of the precision of the GNSS receivers, depending on their location on the nacelle of the wind turbine, and (ii) the determination of the precision of positioning and orientation of the nacelle, and how the precision could be improved by using geometric constraints between the receivers. From the analysis of the time-series of the three GNSS receivers, it was observed that the GNSS receiver with the highest precision (lower standard deviation) was the one located at the tail of the nacelle, which was the GNSS receiver furthest from the wind turbines blades. This was confirmed by the standard deviation of the GNSS Up time-series, which expressed GNSS data noise, as the standard deviation of GNSS receiver sd2 was the lowest, reaching 9 mm, as compared to other two GNSS receivers (sd1 and sd3), which reached 11 mm. Furthermore, it was observed that the GNSS receivers' precision depended also on the rotation speed of the blade since the GNSS data noise increased with the rotation speed of the blade. More specifically, the standard deviation of the GNSS Up time-series of sd1, sd2 and sd3 for time-interval of high speed of blade rotation (from $t = 265$ s to $t = 390$ s) was 14, 11 and 28 mm, respectively, whereas for low speed of the blade rotation (from $t = 2100$ s to $t = 4000$ s) the corresponding standard deviation of sd1, sd2 and sd3 GNSS receivers was 11, 9 and 11 mm, respectively.

Also, the precision of the estimated orientation of the nacelle was investigated by analysing the computed nacelle orientation as derived from the bearing formed by the two pairs of GNSS receivers (sd1-sd3 and sd2-sd3). Based on the two estimations of the nacelle orientation and the geometric constraints between the two formed GNSS pairs, it was observed that the range of the nacelle azimuth estimation could vary about ± 5 degrees, depending also on the rotation speed of the blades. Again, the deviation of the azimuth estimation increased with the rotation speed of the blades. To enhance the precision of the estimated position and orientation of the nacelle, we applied geometric constraints based on the right-angle triangle formed by the three GNSS receivers and their in-between fixed distances and formed angles. We examined the four possible cases where combinations of the formed distances and angles were constrained (i.e. fixed) or non-constrained (i.e. non-fixed) and it was observed that the application of the distance geometric constraints between the GNSS receivers had the main impact, since the precision of the positioning estimation was improved by 1 mm. The highest precision was achieved when the formed distances and the angles between the GNSS receivers were constrained and non-constrained, respectively, as the corresponding error (i.e. standard deviation) in Easting and Northing was 6.6 mm and 7.9 mm, respectively. Furthermore, it was observed that by using the weighted average there was a small improvement on the precision of the estimated Easting and Northing coordinates compared to the averaged results, as the standard deviation was slightly reduced, with the reduction reaching 0.5 mm.

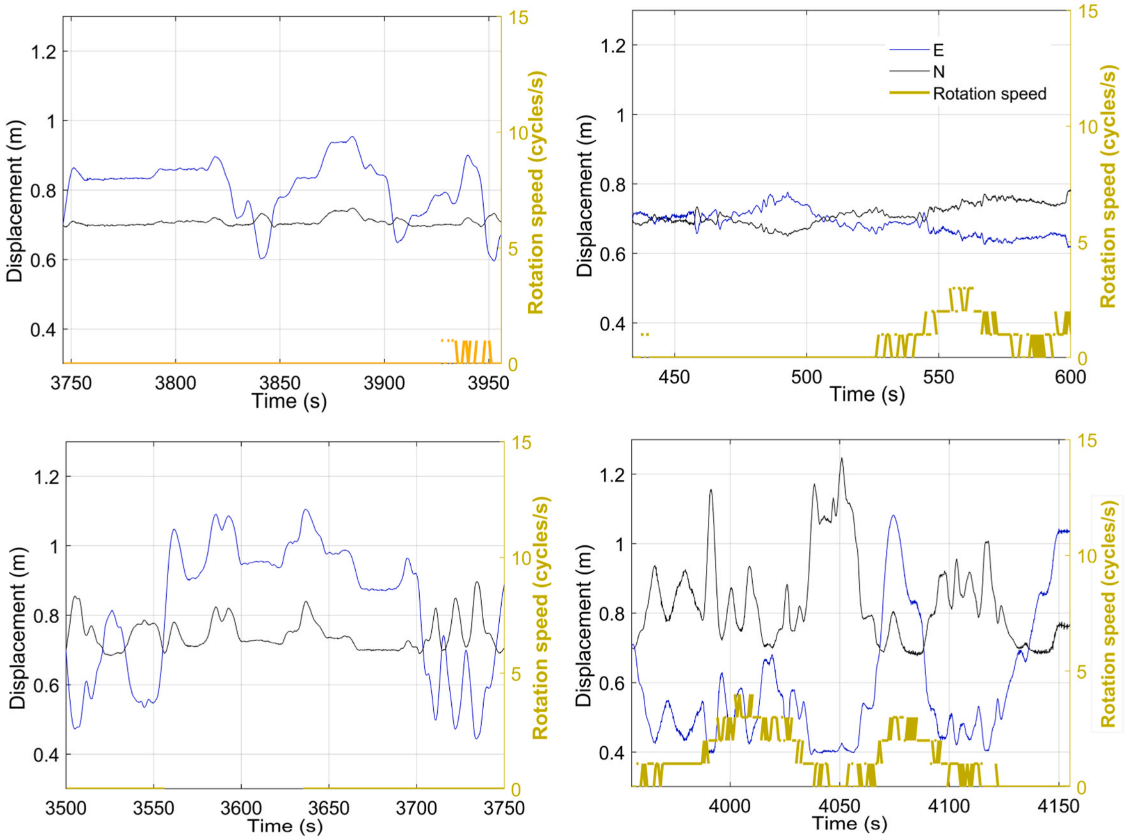

Fig. 11. The timeseries for E/N for sd2 station for 4 different nacelle/blade movement scenarios (Top left: Case A, Top right: Case B, Bottom left: Case C, and Bottom right: Case D).

Finally, the second experimental session focused on the evaluation of the wind turbine operational modes on the performance of the GNSS receivers. We examined the GNSS receiver located at the tail of the nacelle, since the GNSS receiver of this location was expected to have the highest precision. Based on the analysis of the GNSS Easting, Northing and Up time-series, it was observed that the noise of the GNSS data was slightly amplified with the increase of the rotation speed of the nacelle blades, affecting mainly the relatively high-frequency range (>1 Hz). The increase of the white noise level and its frequency context depends not only on the frequency motion of the wind turbine/blade, but also on the angle of incident defined by the satellite, reflecting surface (wind turbine) and the antenna, as observed in previous studies [26,27]. It could also be inferred by comparison between case C and case A or case D and case B that the horizontal rotation of the nacelle might also amplify the GNSS error. To summarise, when the rotation blade and nacelle were both moving, the measurement errors tended to be the largest, followed by the case when rotation blade was moving and nacelle was still, with the least measurement errors when the nacelle and blade were both not moving.

6. Conclusion

In this feasibility study, the precision and performance of GNSS receivers were experimentally evaluated for determining the positioning and orientation of a wind turbine nacelle. The experiments were conducted on a small wind turbine with multiple strategically placed GNSS devices atop the nacelle. By employing the GNSS PPK solution and analysing the GNSS positioning time series (Easting, Northing, Up components), we assessed the performance of the GNSS receivers and examined the effects of turbine motion and receiver placement on their performance.

In the first experiment, the precision of the planar components was estimated to range from 5 to 7 mm when the turbine blades were under rotation, improving to 4 to 6 mm when the turbine blades slowed down or stopped. Similarly, the precision of the Up component improved under these conditions. It was also found that GNSS precision deteriorated as the station approached the rotating blade. Specifically, the precisions of the Up component close to and further away from the blades were approximately 25 mm and 12 mm respectively, during high-speed blade rotation. Hence, the study suggests that GNSS antennas should be located at the nacelle’s tail, away from the blades. Additionally, the study demonstrated that the nacelle’s bearing could be precisely determined using GNSS coordinates (with a precision level of 1.6°) even during varying blade rotation speeds. Using multiple GNSS receivers and considering the geometric constraints between them (i.e., distances between antennas) can further enhance precision.

In the second experiment, the impact of multipath-induced errors was investigated, particularly during blade rotation, which increased white noise levels primarily in the high-frequency domain (>1 Hz). On the other hand, the horizontal rotation of the nacelle could be identified in the lower frequency domain in the E/N spectra.

This study is the first experimental attempt to demonstrate the potential of GNSS technology for monitoring the kinematic behaviour of wind turbine nacelles in positioning and orientation. It highlights key practices for the efficient and reliable application of GNSS receivers. Two main recommendations are i) the location/deployment of the GNSS antenna at the tail of the nacelle, and ii) the application of geometric constraints for two or more GNSS receivers to reduce GNSS measurements noise, such as multipath-induced error due to proximity to the rotation blade(s) and interference errors due to proximity between GNSS antennas [28]. Future research should focus on applying GNSS to monitor large-scale wind turbines, aiming to evaluate GNSS performance in tracking nacelle responses (i.e., positioning, orientation, yaw motion) and accurately estimating deformation characteristics (i.e.,

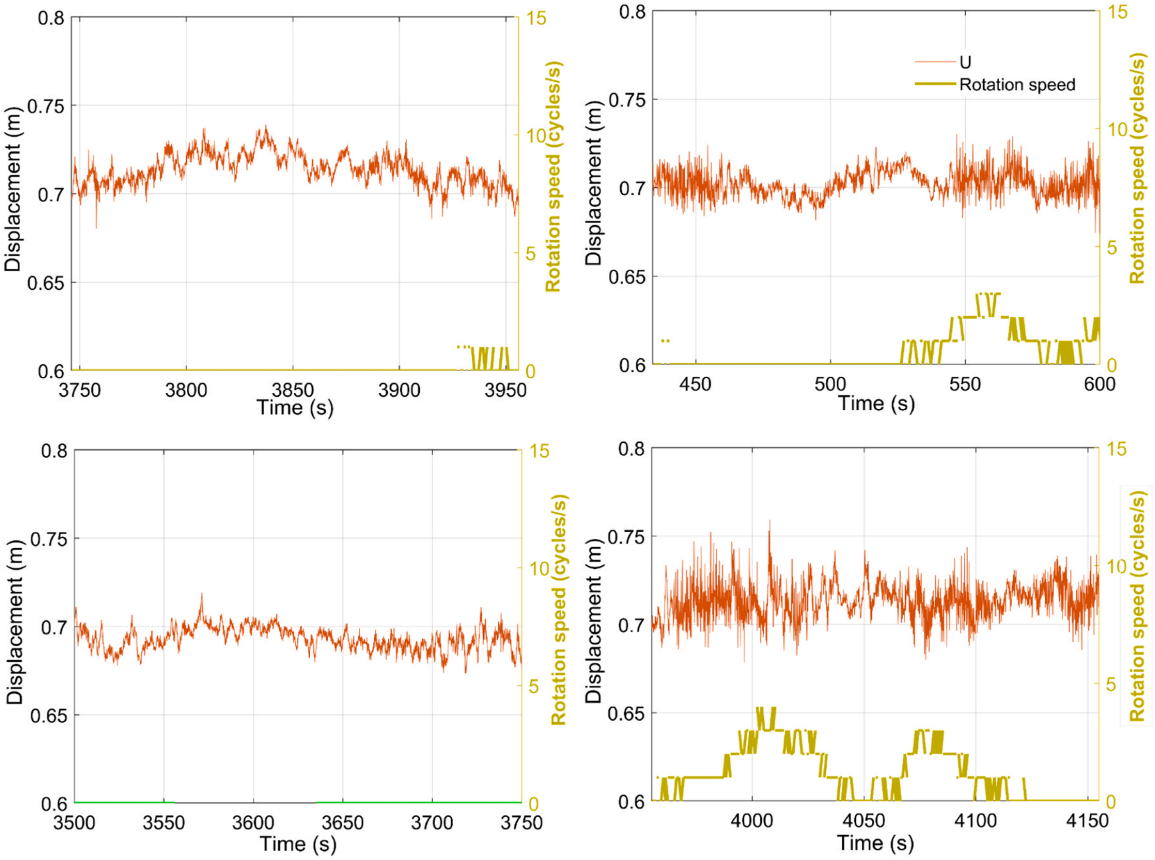

Fig. 12. The timeseries for Up component for sd2 station for 4 different nacelle/blade movement scenarios (Top left: Case A, Top right: Case B, Bottom left: Case C, and Bottom right: Case D).

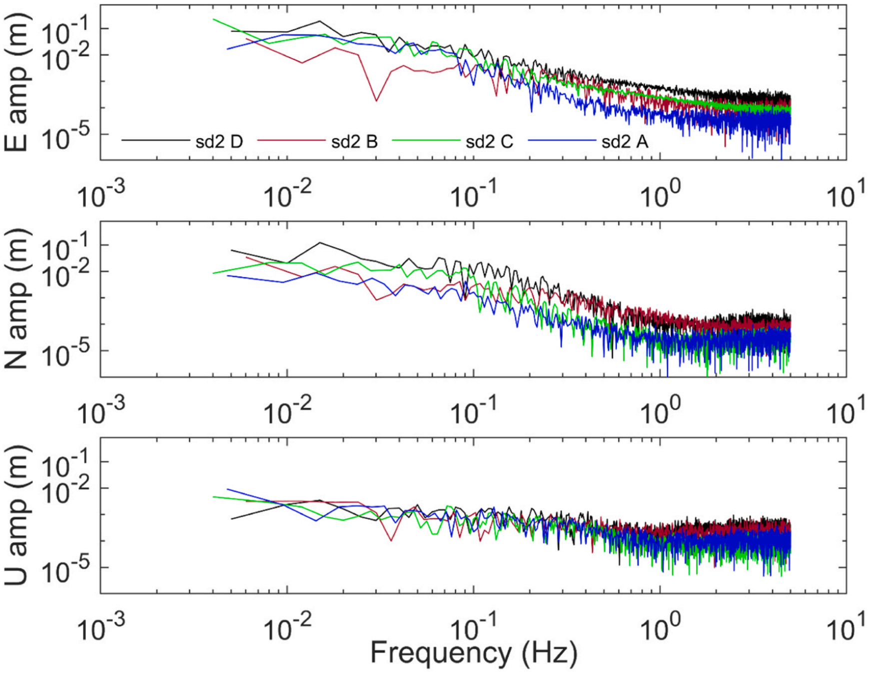

Fig. 13. The Discrete Fourier Transform (DFT) analysis for different cases for E/N/U components for station sd2.

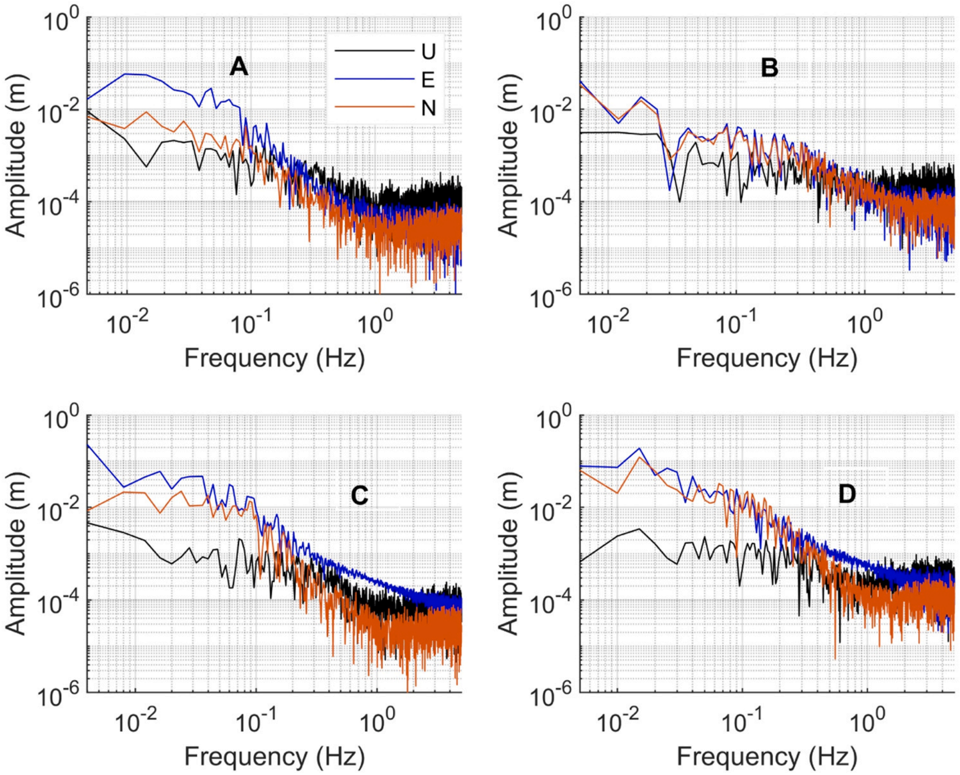

Fig. 14. The Discrete Fourier Transform (DFT) analysis for different cases (A, B, C, D) for E/N/U components for station sd2.

displacement, frequency) under various wind load conditions and operational modes.

CRediT authorship contribution statement

Chendong Li: Writing – review & editing. **Yuchen Yang:** Writing – review & editing. **Paul Bhatia:** Writing – review & editing. **Xu Tang:** Supervision, Conceptualization. **Yiru Li:** Data curation. **Francis Xavier Ochieng:** Writing – review & editing. **Craig Matthew Hancock:** Writing – review & editing, Supervision, Resources, Project administration, Investigation, Funding acquisition, Data curation, Conceptualization. **Panos Psimoulis:** Writing – review & editing, Supervision, Methodology, Conceptualization. **Chenyu Xue:** Writing – review & editing, Writing – original draft, Visualization, Software, Methodology, Formal analysis.

Declaration of Competing Interest

The authors declare that they have no known competing financial interests or personal relationships that could have appeared to influence the work reported in this paper.

Data availability

Data will be made available on request.

References

[1] Martinez-Luengo M, Kolios A, Wang L. Structural health monitoring of offshore wind turbines: a review through the statistical pattern recognition paradigm. Renew Sustain Energy Rev 2016;64:91–105.
[2] Ozbek M, Rixen DJ. Operational modal analysis of a 2.5 MW wind turbine using optical measurement techniques and strain gauges. Wind Energy 2013;16(3):367–81.
[3] Currie M, Saafi M, Tachtatzis C, Quail F. Structural integrity monitoring of onshore wind turbine concrete foundations. Renew Energy 2015;83:1131–8.
[4] Avendano-Valencia LD, Chatzi EN, Tcherniak D. Gaussian process models for mitigation of operational variability in the structural health monitoring of wind turbines. Mech Syst Signal Process 2020;142:106686.
[5] Karami MA, Farmer JR, Inman DJ. Parametrically excited nonlinear piezoelectric compact wind turbine. Renew Energy 2013;50:977–87.
[6] Moradi M, Sivoththaman S. MEMS multisensor intelligent damage detection for wind turbines. IEEE Sens J 2014;15(3):1437–44.
[7] Kim S-W, Kang W-R, Jeong M-S, Lee I, Kwon I-B. Deflection estimation of a wind turbine blade using FBG sensors embedded in the blade bonding line. Smart Mater Struct 2013;22(12):125004.
[8] Ou Y, Tatsis KE, Dertimanis VK, Spiridonakos MD, Chatzi EN. Vibration-based monitoring of a small-scale wind turbine blade under varying climate conditions. Part I: An experimental benchmark. Struct Control Health Monit 2021;28(6):e2660.
[9] Barber S, Deparday J, Marykovskiy Y, et al. Development of a wireless, non-intrusive, MEMS-based pressure and acoustic measurement system for large-scale operating wind turbine blades. Wind Energy Sci 2022;7(4):1383–98.
[10] Smarsly K, Hartmann D, Law KH. An integrated monitoring system for life-cycle management of wind turbines. Int J Smart Struct Syst 2013;12(2):209–33.
[11] Psimoulis P, Pytharouli S, Karambalis D, Stiros S. Potential of Global Positioning System (GPS) to measure frequencies of oscillations of engineering structures. J Sound Vib 2008;318(3):606–23.
[12] Psimoulis PA, Stiros SC. Experimental assessment of the accuracy of GPS and RTS for the determination of the parameters of oscillation of major structures. Comput Civ Infrastruct Eng 2008;23(5):389–403.
[13] Xue C, Psimoulis PA. Monitoring the dynamic response of a pedestrian bridge by using low-cost GNSS receivers. Eng Struct 2023;284:115993.
[14] Yu J, Meng X, Yan B, Xu B, Fan Q, Xie Y. Global Navigation Satellite System-based positioning technology for structural health monitoring: a review. Struct Control Health Monit 2020;27(1):e2467.
[15] Meng X, Nguyen DT, Owen JS, Xie Y, Psimoulis P, Ye G. Application of GeoSHM system in monitoring extreme wind events at the forth Road Bridge. Remote Sens 2019;11(23):2799.
[16] Msaewe HA, Psimoulis PA, Hancock CM, Roberts GW, Bonenberg L. Monitoring the response of Severn Suspension Bridge in the United Kingdom using multi-GNSS measurements. Struct Control Health Monit 2021;28(11):e2830.
[17] Maes K, De Roeck G, Lombaert G. Motion tracking of a wind turbine blade during lifting using RTK-GPS/INS. Eng Struct 2018;172:285–92.
[18] Ren Z, Skjetne R, Jiang Z, Gao Z, Verma AS. Integrated GNSS/IMU hub motion estimator for offshore wind turbine blade installation. Mech Syst Signal Process 2019;123:222–43.
[19] Caterino N, Pugliano G, Spizzuoco M, Robustelli U. Variable dampers to mitigate structural demand to wind turbines: the role of the monitoring system features for the effectiveness of the control strategy. Appl Sci 2020;10(7):2498.

[20] Rossi Y, Tatsis K, Awadaljeed M, et al. Kalman filter-based fusion of collocated acceleration, GNSS and rotation data for 6C motion tracking. Sensors 2021;21(4):1543.

[21] Moschas F, Psimoulis PA, Stiros SC. GPS/RTS data fusion to overcome signal deficiencies in certain bridge dynamic monitoring projects. Smart Struct Syst 2013;12(3-4):251–69.

[22] Visual Crossing Corporation. Visual Crossing Weather (2020).[data service]. 2024. Available from ⟨https://www.visualcrossing.com/⟩.

[23] Development of the low-cost RTK-GPS receiver with an open source program package RTKLIB. In: Proceedings of the International symposium on GPS/GNSS. International Convention Center Jeju Korea Seogwipo-si, Republic of Korea; 2009

[24] Xue C, Psimoulis PA, Meng X. Feasibility analysis of the performance of low-cost GNSS receivers in monitoring dynamic motion. Measurement 2022;202:111819.

[25] Pratt V. Direct least-squares fitting of algebraic surfaces. AACM SIGGRAPH computer graphics 1987;21(4):145–52.

[26] Peppa I, Psimoulis P. Detection of GNSS antenna oscillatory motion and multipath conditions via exploitation of multipath-induced SNR variations. GPS Solut 2023;27(3):117.

[27] Bilich A, Larson KM. Mapping the GPS multipath environment using the signal-to-noise ratio (SNR). Radio Sci 2007;42:1–16. https://doi.org/10.1029/2007rs003652.

[28] Peppa I, Psimoulis P, Meng X. Using the signal-to-noise ratio of GPS records to detect motion of structures. Struct Control Health Monit 2018;25(2):e2080. https://doi.org/10.1002/stc.2080.